



IMaging-based CUSTOMised EYE diagnostics

Project ID: 779960

Funded under: H2020-EU.2.1.1. - INDUSTRIAL LEADERSHIP - Leadership in
enabling and industrial technologies - Information and Communication
Technologies (ICT)

Deliverable D7.1 Report on impact of treatment parameters on simulated outcomes



This project has received funding from the *European Union's Horizon 2020* research and innovation programme under grant agreement No 779960.

Document control information	
Title	Report on the impact of treatment parameters on simulated outcomes
Contributing partners	Optimo, ULiv
Type	REPORT
Dissemination level	<input checked="" type="checkbox"/> CO Confidential, only for members of the consortium (including the Commission Services) <input type="checkbox"/> RE Restricted to a group specified by the consortium (including the Commission Services) <input type="checkbox"/> PP Restricted to other programme participants (including the Commission Services) <input type="checkbox"/> PU Public
Status	<input checked="" type="checkbox"/> Draft <input type="checkbox"/> WP Manager accepted <input type="checkbox"/> Co-ordinator accepted
Due date	2021-09-30
Delivery date	2022-01-26
Action requested	<input type="checkbox"/> to be revised by Partners involved in the preparation of the deliverable <input type="checkbox"/> to be reviewed by applicable IMCUSTOMEYE Partners <input type="checkbox"/> for approval of the WP Manager <input type="checkbox"/> for approval of the Project Coordinator

Revision history			
Version	Date	Author	Comment
<1.0>	2021-12-03	Harald Studer	Initial version
<2.0>	2021-12-08	Ahmed Abass	ICRS section
<3.0>	2021-12-09	Ahmed Elsheikh	Report drafting
<4.0>	2021-12-13	Frederik Theler	Added refractive surgery section and results optimo
<5.0>	2022-01-25	Harald Studer	Final version



Table of contents

1	Summary.....	4
2	Introduction.....	4
3	Material and methods.....	5
3.1	Biomechanical model for corneal tissue	5
3.2	Modeling of material inhomogeneity over depth	5
3.3	Finite element simulation details	7
3.4	Mesh pre-stressing	8
3.5	Refractive surgery simulations	8
3.6	Cataract surgery simulations.....	10
3.7	Intra-Corneal ring segment surgery simulation	10
4	Results.....	12
4.1	Refractive surgery simulations	12
4.2	Cataract surgery simulations.....	15
4.3	ICRS Keratoconus model validation.....	16
5	Conclusions	17
6	References.....	18



1 Summary

Finite element modeling of the human cornea was conducted to obtain a deeper understanding on three commonly performed ophthalmic-surgical treatments. Thereby, surgical parameters, as well as corneal stiffness values were varied in order to obtain parametric study results. A sophisticated mathematical formulation, including the collagen fiber ultrastructure, was used to describe the biomechanical behavior of the soft biological tissue. The simulated treatments include cuts into the corneal tissue, an implant inside a pocket and specific removal (ablation) of tissue. The overall goal of these parametric simulations was the assessment of the expected variation in surgical outcome, based on varying tissue stiffness values. Simulation work on all three different treatment models proved to be challenging tasks numerically. Simulation results suggest that surgical outcome only little depends on stiffness variations of corneal tissue. Some technical challenges remain to be solved, before reliable software packages can be made ready to be used by clinical staff for patient-specific surgery planning.

2 Introduction

Cataract, arcuate keratotomy surgery: Traditional cataract surgery, manually executed with a scalpel in combination with phaco emulsification has long been the standard treatment for Cataract senil, an age-related opacification of the crystalline lens. In recent years, femto-second laser technology has been employed more often to cut the access tunnels, as well as for lens fragmentation (reducing the need for the potentially harmful phaco-energy during surgery). Using the femto-second laser platform opens the option to correct preoperative astigmatism through arcuate keratotomy – small arc-like incisions in the corneal periphery, in the course of Cataract surgery. In contrast to manual arc-incisions, femto-second laser arcuate keratotomy shows better long-term stability of the correction (internal data at Optimo Medical AG). However, studies show a considerable degree of remaining astigmatism after laser arcuate keratotomy (Day et al 2016). This report investigates the question, whether this remaining clinical variability might stem from variability in biomechanical properties of the operated corneas, by running parametric simulations.

Refractive surgery: Laser Assisted In-Situ Keratomileusis (LASIK) has become the most prevalent refractive surgical procedure for myopic and hyperopic corrections (about 1.2 million procedures a year in the US) – over the last two decades. Patient satisfaction is generally very high – between 92 and 98 percent (Tahzib 2005, Bailey2002, McGhee2000). Modern excimer laser systems are capable of restoring 20/20 uncorrected visual acuity (UCVA) in myopic eyes up to -10D and hyperopic up to +6D, feature tissue saving procedures (Hashemi2010), provide patient-specific, topography guided ablation patterns, and can treat astigmatism with elliptically shaped patterns. While smaller refractive corrections (< 5.0D) tend to be highly predictable, higher dioptric changes show more variability in surgical results. By running parametric simulations, this report investigates the question, whether this remaining clinical variability might stem from variability in biomechanical properties of the operated corneas.

Intra Corneal Ring Segment Keratoconus surgery: Keratoconus is a progressive pathology where a growing bulge in the cornea starts to impair vision and untreated can result in a corneal transplantation to save the eye. The most common treatment is crosslinking where the cornea gets stiffened in order to halt the progression. One of the



most recent approaches for treating keratoconus is the use of intracorneal ring segments (ICRS) implantation (Kanellopoulos et al., 2006). Moderate keratoconus cases where disease cone progression has halted can be treated effectively using ICRS (Izquierdo et al., 2019). ICRS are small polymethyl-methacrylate (PMMA) arc-shaped devices that are implanted into pockets inside the cornea to stress it in a way that flattens its central surface, hence reducing the eye's refractive error and improving visual acuity (VA) (Sakellaris et al., 2019). ICRS is a practical option for patients whose best-corrected VA (BCVA) with spectacles is too low or cannot tolerate contact lenses because of underlying ocular allergy to disinfecting solutions or any other systemic conditions.

ICRS flattens the corneal central surface by altering the stress equilibria in the collagen lamellae, achieved by applying pressure and taking up space. Unlike refractive surgery, ICRS have the advantage of being reversible and allowing the cornea to return to its original shape once removed (Corbett et al., 2019). With all of the previously mentioned benefits, ICRS based treatments protocols are based on empirically conceived nomograms that have been developed as a result of processing unpublished clinical data using non-mathematically validated techniques (Sakellaris et al., 2019). Hence, the current report presents a study that fills this gap in knowledge by presenting a clinically validated mathematical model for ICRS based treatments that helps to understand why certain protocols work better than others and opens the horizon to develop scientifically-backed ICRS protocols that are predictable and offer foreseeable vision correction.

3 Material and methods

3.1 Biomechanical model for corneal tissue

All mechanical properties of ocular tissues are based on a biomechanical material law for ocular soft tissue. The law attributes for the tissue's incompressibility and its material inhomogeneity in-plan and over its thickness. The tissue's high degree of directional dependence, along with its shear-stiffness, caused by cross-links, is both included in the material through continuum mechanical anisotropies as well as further factors and complex boundary conditions. In this project, we employed the previously published biomechanical model, which used additive terms in a strain energy function to describe above mentioned tissue characteristics:

$$\Psi = U + \bar{\Psi}_m[C_{10}] + \frac{1}{\pi} \int \Phi \cdot (\bar{\Psi}_{f1}[\gamma_m, \mu_m] + \bar{\Psi}_{f2}[\gamma_k, \mu_k]) d\theta, \quad (1)$$

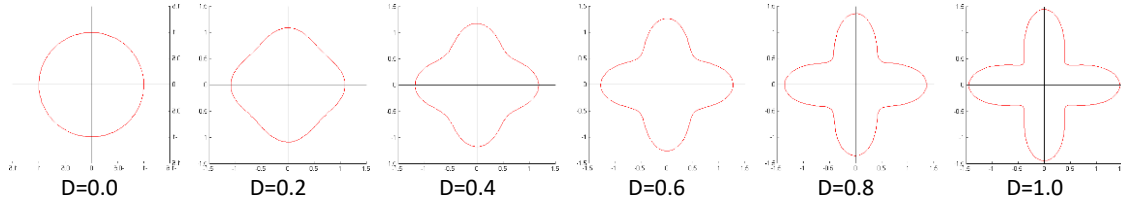
Thereby, C_{10} , γ_m , μ_m , γ_k , and μ_k are material constants, varying with age or measured patient-specific mechanical properties. This law is implemented into the Mechanical finite element package (Ansys Inc, Canonsburg, Pennsylvania, US) and was inversely fitted to multiple sets of experimental data (Studer et al., 2012). As a result, the obtained sets of material coefficients allow the adaptation of the mechanical behavior to the patients' age or measured properties of individual corneas. It can be used to simulate and predict the results of a wide variety of mechanical interactions with the human cornea.

3.2 Modeling of material inhomogeneity over depth

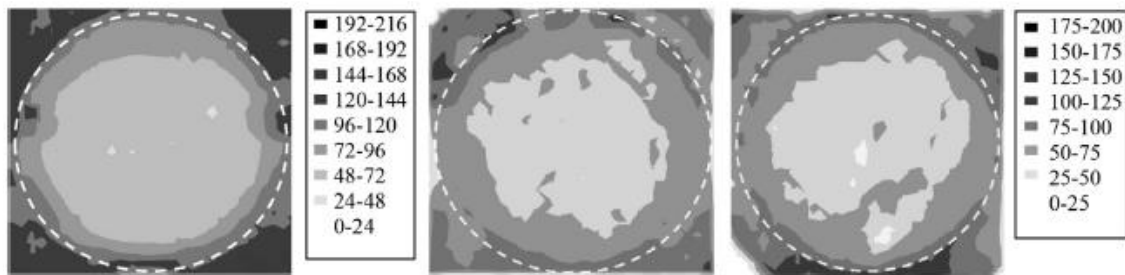
This section explains how material properties are modeled and varied over the thickness profile of the cornea:



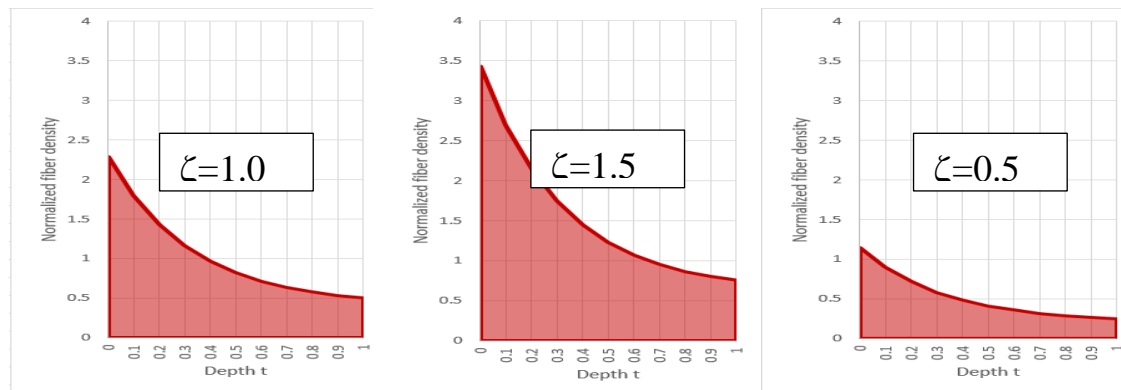
Anisotropy: Collagen fibre anisotropy is varied over thickness profile (according to Abahussin et al. 2009). Thereby, dominant fibre directions (horizontal/vertical) are most pronounced in deep corneal layers. The anterior stroma shows an almost isotropic distribution of fibres. The following images show fibre distribution in the centre of the cornea (D =depth, where $D=0$ is anterior stromal surface):



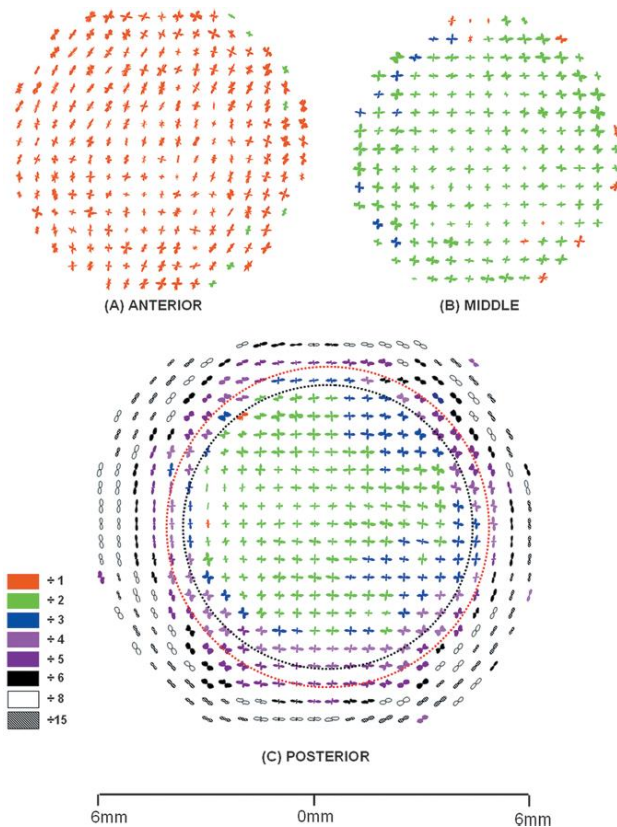
Density: En-face fibre density distribution is modelled according to Whitford et al (2015) and is decreased with corneal thickness. As shown in Whitford et al. 2015, collagen fibre density is not uniform in the human cornea. Whitford further presented mathematical modelling, allowing the incorporation of density distribution into the strain energy formulation. The following images show fibre distribution of three specimens from Whitford et al (2015):



From Whitford's mathematical formulation, fibre density at a specific point in the cornea is given by ζ . The following images show how the density is modelled depth dependent:



The three plots represent three different density “situations” (1.0, 1.5, and 0.5). It is clear, that for any density value, the most anterior point in the stroma is the stiffest (representing Bowman's membrane).



Cross-links: Shear-stiffness of the tissue is dominated by links between the fibres (cross-links). They decrease over corneal depth (according to Randelmann et al, 2008; Sondergaard et al. 2013; and Sloan et al. 2014), resulting in a more and more cleanly stacked organization, the deeper in the cornea. This is confirmed in literature as shear stiffness decreases from anterior towards posterior (Petsche et al. 2012, Randelmann et al. 2008, Scarcelli et al. 2012).

The image on the left is from Abahussin et al. 2009 and shows results from x-ray scattering crystallography from three different corneal tissue layers.

3.3 Finite element simulation details

Finite-element simulations contain a finite-element model of the human cornea, and a 4mm wide scleral rim attached to it. The following table shows general simulation model details:

FEM Package	ANSYS Structural 17.1
Optimeyes	Optimeyes 2.1 simulation and post-processing
Element type	8-noded bricks, large deformation, linear integration, hybrid formulation
#Elements	> 100'000. Uniform density. Throughout 8 layers of elements.
Model	Part-eye model with cornea, and parts of the sclera (clamped for boundary cond.)
IOP	Patient specific IOP (if applicable in the project), otherwise 15mmHg
Biomechanical properties	Optimo proprietary material law: hyper-elastic, non-linear, incompressible, anisotropic, in-homogeneous, equation with collagen fibers and cross-links
Assumptions	Non-full eye model; frictionless sliding between layers in case of incisions, implants, or other contacts; constant IOP for pre- and postop;



3.4 Mesh pre-stressing

Since topography and anterior segment tomography devices, such as the Pentacam (Oculus Optikgeräte GmbH, Wetzlar, Germany), the Galilei (Ziemer Ophthalmology, Biel, Switzerland), or the Orbscan (Bausch&Lomb Technolas, Munich, Germany), measure corneal geometry in-vivo, the corneal tissue is under mechanical stress, and the shape in the absence of acting forces is *a priori* not known. An iterative approach to pre-stress the model, extending to the one proposed by Pandolfi et al., 2008, is used. Thereby, the algorithm searches for the stress-free shape of the patients' cornea such, that after applying pressure inside the eye-model (in the simulation), the original shape as measurement with the tomography device is reproduced.

3.5 Refractive surgery simulations

For refractive surgery simulation the Femto-LASIK (Laser-in-situ-Keratomileusis) treatment was modeled. This is a two step process where the Femtosecond laser is used to cut a fine three-dimensional profile, the flap, into the outermost layers of the cornea. The flap consists of a circular area which is cut at a constant depth of usually between 110 μ m and 130 μ m, and a nearly circumferential cut, circumcising the border of this area. This allows lifting of the partially separated flap (Figure 1), and hence exposes a stromal surface. The flap is still attached at the hinge and will be placed back in its old position after the completion of the surgery, to close the cornea again.

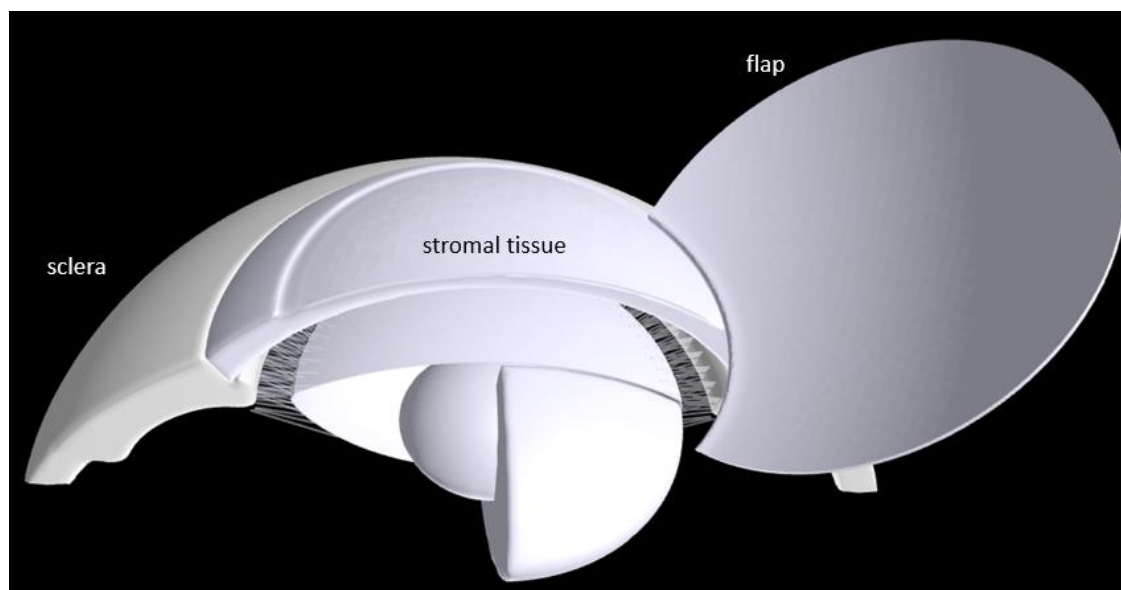


Figure 1 Visualization of the thin flap opened and the exposed stromal tissue. The femtosecond laser is able to cut out this 3-dimensional profile, afterwards the excimer laser can work on the stromal surface and evaporate tissue with high precision.

The flap is removed in order to keep the outermost, 55 μ m thick epithelium cell layer intact, while at the same time establishing a favorable surface for the excimer laser to achieve high precision. The excimer laser procedure immediately follows after lifting the flap, and does evaporate stromal tissue to achieve the desired refractive correction. Depending on the refractive target, the ablated profile either steepens or flattens the central part of the cornea. An approximation of the Munnerlyn formula (eq. 2) was used to define the ablation profile for the simulations. The formula it returns the ablation depth, as a function of the amount of target correction in dioptries (d), and radial position (r).



$$\text{ablation depth } (r, d) = \frac{(2r)^2 d}{3} \quad (2)$$

The simulated procedure closely follows the actual surgical procedure, except for the fact that the flap doesn't need to be lifted before removing the ablation profile. During the simulated treatment the flap gets cut (planar and near-circumpherential cut at the border of the flap) and the ablation profile (see Figure 2) is removed from the model. A frictionless contact definition between the posterior flap surface and the anterior stromal surface underneath the ablation is introduced, allowing the two surfaces to slide but – modeling cohesion effects - restricting them to stay in closed contact (see Figure 3). Afterwards, the intraocular pressure is applied on the inside of the model. After the simulation has completed, the resulting elevation information from anterior and posterior corneal surface are exported as 3D point clouds, and can then be evaluated within the Optimeyes™ software.

The Femto-LASIK model was built to perform parametric studies, analyzing the impact and sensitivity of various parameters. Thus the depth and size of the flap, the size of the hinge and the ablation profile can be altered to assess the impact of said parameters on the simulation outcome.

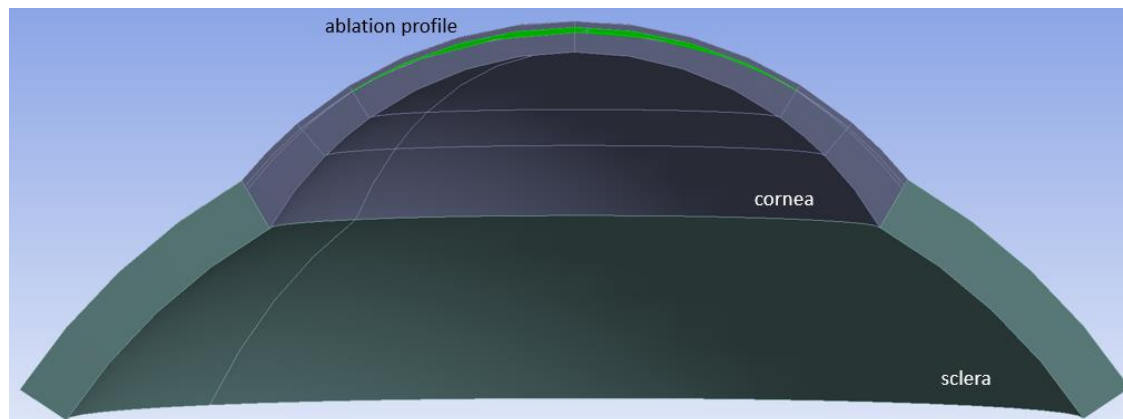


Figure 2 Cross-sectional view of the refractive surgery model showing the ablation profile in green color. It is removed during the multi step process of simulating the Femto-LASIK treatment.

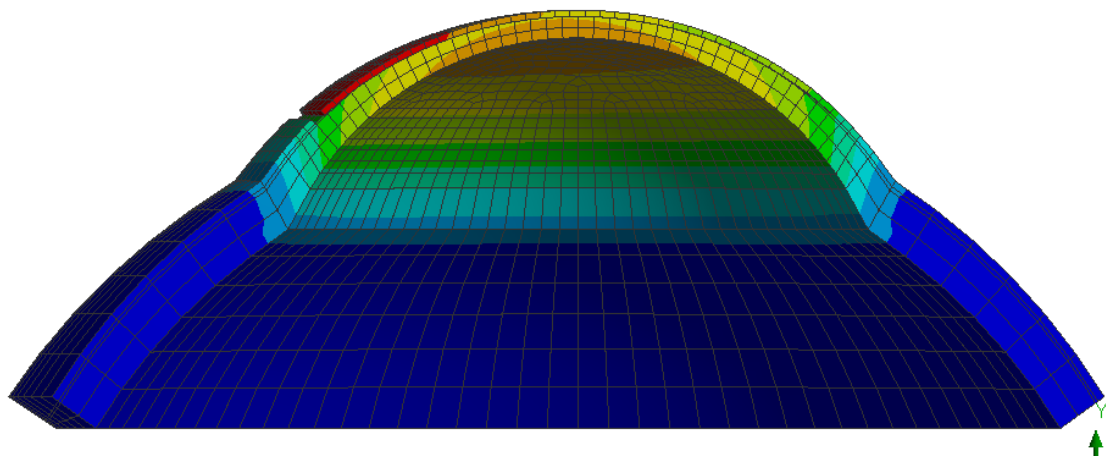


Figure 3 After the ablation profile is removed, contact is established between the posterior flap and the remaining stromal anterior surface. A small gap can be seen on the left side where the flap was cut, this is due to two reasons, the first being that the flap tissue is no longer under tension and contracts back to a relaxed state. Further the overall thickness of the cornea got thinner in the center, thus its strength is reduced yielding into a slight bulging "outwards" in comparison to before the treatment.



3.6 Cataract surgery simulations

In this project, astigmatism correction by arcuate keratotomy, in the course of Cataract surgery was simulated. Thereby, the phaco tunnel was assumed to have a relatively small impact of 0.25D (surgically induced astigmatism), and the arcuate incisions were simulated using the finite element method. Figure 4 depicts the modeling process for the finite element model for arcuate keratotomy Cataract surgery. After the 3D constructions are concluded, the software package generates a spherical finite-element mesh, which was then transformed (warped) to obtain the initially specified shape (eg. patient-specific corneal shape). This process is fully automatic with the Optimeyes™ software package. Thereby, the warping algorithm transforms template spherical models such, to match the Zernike decompositions $W(r,\theta)$ (Zernike 1934) of the anterior and posterior corneal surface, as well as the Pachymetry of the topography measurement. Zernike polynomials up to order 12 have been used for all cases, and the warping algorithm typically works at an error-level of less than one micron.

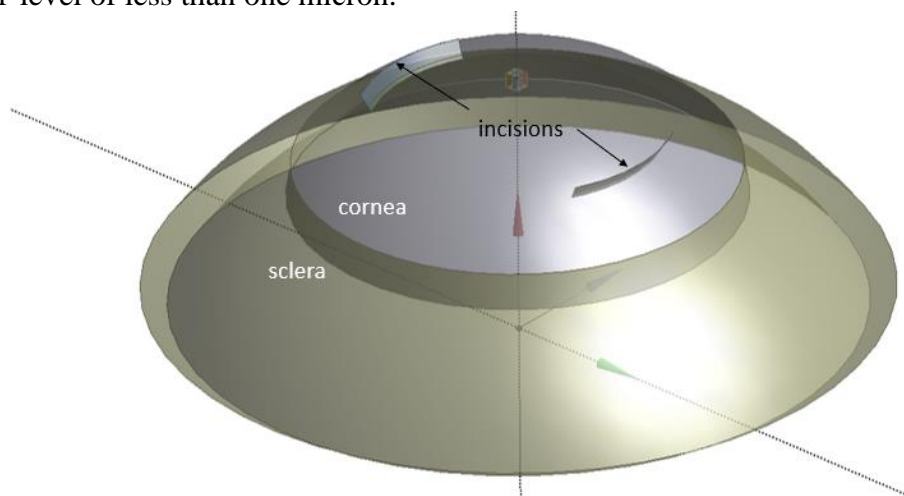


Figure 4 The modeling steps of the FE simulation models in ANSYS Structural 17.1 start with the construction of a 2D profile of the cornea and the sclera. From that, a full 3D construction of the model, with the 4mm scleral rim attached to it is created. The arcuate incisions, applied during Cataract surgery, were modeled and placed in the 3-dimensional construction before finally, the model was meshed. The image on top is a 3D view of the model showing the cornea and the scleral rim.

3.7 Intra-Corneal ring segment surgery simulation

Clinical data

The study utilised a fully anonymised record of 38 clinical cases of ICRS fittings in solely secondary analyses. Cases were aged 32 ± 15 years and ranged from 12 to 73 years with 21 right eyes and 17 left eyes. Only complete records were selected from a bigger anonymised data set where cases with a full record of topography and ICRS information were considered. No clinical data were collected specially for this study; therefore, no ethical approval was required. Nevertheless, the study was conducted following the standards set in the Declaration of Helsinki.

Data processing

A custom-built fully automated MATLAB code was built as part of the current study, the code automatically reads the topography data of the clinical cases one by one. Raw elevation height data was extracted from the Pentacam HR tomography Scheimpflug



imaging system over a squared mesh grid of 141 points in each direction covering the range of -7 to 7 mm in steps of 0.1 mm. Both anterior and posterior surfaces were extracted with the same cartesian X, Y coordinates while the Z coordinate was different for each surface and had a direction aligned to the eye axis with a positive direction towards the Pentacam fixation target.

As the eye's surface data is usually collected in a tilted position as a result of the foveal centre, the most sensitive part of the retina, being located 2.5 mm temporal to the eye axis (Gross, 2005), 3.4 mm temporal to the optic disk (Kolb H, 1995), and marginally inferior. This geometrical fact forces the brain to rotate the eye to a tilted position to refract light rays towards the fovea. Therefore, the MATLAB code applies an optimisation method to locate the eye's optical axis. This location was achieved by modelling parallel light rays refracting through the cornea's anterior and posterior surfaces following Snell's law (Smit and Atchison, 1970; Smith, 2000). The path of the refracted ray was determined as it passed through the cornea with the refractive indices of air ($n=1.0$), corneal tissue ($n=1.376$), and aqueous ($n=1.336$) (Smit and Atchison, 1970; Vojnikovi and Tamajo, 2013). As the optical axis is defined as a straight light ray that enters and leaves an optical system (the eye refractive surfaces in this case) along the same line without refraction (Arba Mosquera, Verma and McAlinden, 2015), the path for that light ray may be located between two points on the corneal anterior and posterior surfaces. According to Snell's law, ideally, normal vectors to both corneal anterior and posterior surfaces are almost identical on the optical axis. Hence, normal vectors to the corneal anterior and posterior surfaces were determined, then squared differences were added and then the average of the two normal vectors with minimum squared differences summation was used as the optimal optical axis. This approach is detailed in Lopes et al. optimisation-based optical axis determination method published recently (Lopes et al., 2021).

To be able to apply sensible boundary conditions that allow an accurate simulation without affecting the ICRS fitting process, corneal surfaces were extended 2 mm beyond the Pentacam measured range using 5th order Zernike polynomials to a mesh grid covering a radius of 10 mm in steps of 0.05 mm and 360° in steps of 0.5° . This process was based on averaged scleral geometry as reported in (Consejo, Wu and Abass, 2020) and the limbus averaged 3D location as reported in (Moore et al., 2020).

This allows the cornea to be held (restrict its displacement) from its extended edge without affecting its central or peripheral zones during the simulation process. After the extrapolation process, original surface pieces of data were placed back into their positions to diminish the effect of the extrapolation on the originally measured surfaces. Extrapolated portions of corneal surfaces were not used in the FE model validation process or any analyses steps beyond FE modelling.

At this stage, the MATLAB code constructs the eye's FE mesh, nodes, element file, input file and material files automatically. Accurate nodes positioning has been achieved using nonparametric cubic spline fitting in the three-dimensional (3D) domain while the element construction process was achieved by using linear sequencing.

ICRS implant was built as the MATLAB code reads a text setup file prepared for each case. The setup file contains the number of implants, the implant arc length, the implant thickness, depth ratio, width and diameter. The code generates the implant node and element files automatically and makes the Abaqus FE simulation ready before running it.

Finite element modelling

FE models built in this study consisted of three-dimensional 8-noded solid hybrid elements (C3D8H) in 2 layers for the cornea and one layer for the ICRS. The corneal edge nodes were restricted in all directions as a boundary condition for the simulation.



Analyses were carried out in ABAQUS 6.14 (Dassault Systèmes, Vélizy-Villacoublay, France) FE software package licenced to the University of Liverpool, UK.

The internal surface of the eye was defined as an element-based surface and the internal pressure was applied statically in a normalised time-stepped scale. The eye's stress-free geometry (at intraocular pressure IOP=0 mmHg) was achieved when eye globe models were primarily built using the pressurised eye measurements, then a stress-free adaptation of each model was determined by following the iterative method presented in (Elsheikh et al., 2013). In each case, the stress-free model was computed by considering IOP as measured by Corvis ST (Wang et al., 2018) and a maximal error in node position less than 10-4 mm. Once the stress-free models were determined, they were pressurised to IOP pressure to mimic the aqueous and vitreous effects and simulate physiological IOP. The study analyses were carried out using the implicit integration scheme with the ABAQUS "NLGEOM" nonlinear geometry option set to "ON" during the simulation process.

The eye's biomechanically corrected IOP (bIOP) and material properties were determined from the stress-strain index (SSI) (Zhang et al., 2021) that has been provided via Corvis ST. Incompressible, isotropic material behaviour was applied (Elsheikh et al., 2007; Whitford et al., 2016) along with a first-order (N=1) Ogden material hyperelastic model in the FE modelling. The used Ogden constitutive strain energy equation can be expressed in terms of the principal stretches (ratio between the deformed length and the initial length in each principal direction) as

$$U = \sum_{i=1}^N \frac{2\mu_i}{\alpha_i^2} (\bar{\lambda}_1^{\alpha_i} + \bar{\lambda}_2^{\alpha_i} + \bar{\lambda}_3^{\alpha_i} - 3) \quad \text{Eq.1 (Ogden and Hill, 1972)}$$

Where U is the strain energy; μ_i and α_i , are the nonlinear material's parameters; $\bar{\lambda}_1$, $\bar{\lambda}_2$ & $\bar{\lambda}_3$ are the deviatoric principal stretches in principal directions. Hence the relevant principal stresses can be calculated as

$$\sigma_1 = \frac{\partial U}{\partial \bar{\lambda}_1} \quad \sigma_2 = \frac{\partial U}{\partial \bar{\lambda}_2} \quad \sigma_3 = \frac{\partial U}{\partial \bar{\lambda}_3} \quad \text{Eq. 2 (Ogden and Hill, 1972; Bower, 2009)}$$

On the other hand, ICRS material was simulated as rigid elastic components with a modulus of elasticity of 3000 MPa and a Poisson ratio of 0.3.

Abaqus FE simulation was carried out in three stages. In stage one, stress-free analysis was carried out and the unstressed geometry was calculated. During stage two, IOP was applied while the implant pocket was opened by a pressure of 1.5 IOP selected based on a preliminary study. ICRS was then inserted into its position and the model was deflated while the ICRS displacement was initially restricted in all directions. In the third stage, IOP was applied while the ICRS was free to move in all directions. Once the simulation finished, Python scripts were used to extract the results. All stages were triggered automatically through the MATLAB custom-built code.

4 Results

4.1 Refractive surgery simulations

The finite element mesh used for prestressing was a spherical shaped model, which was used for the simulation of a myopic femto-LASIK treatment. The biomechanical stiffness, called *overall stiffness*, was varied to simulate stiffer and softer specimen. Thereby, variability in stiffness followed the expected bandwidth from clinical SSI (stress-strain-index) measurement values by Corvis ST or the future OCT device developed in the



IMCUSTOMEYE project. The other model parameters that were varied in this simulation project were the ablation profile, as well as flap depths and flap diameter. Thereby, the ablation profiles were ranging from -1.0D to -5.0D (low to high), flap depths from 110 μ m to 150 μ m and flap diameters from 110 μ m to 150 μ m.

Figure 5 shows anterior axial curvature maps of the model before and after the simulation. Curvatures are represented by color-coded values between 10.0D and 90.0D. The maps after the simulation are for a low myopic ablation profile, and for a high myopic profile.

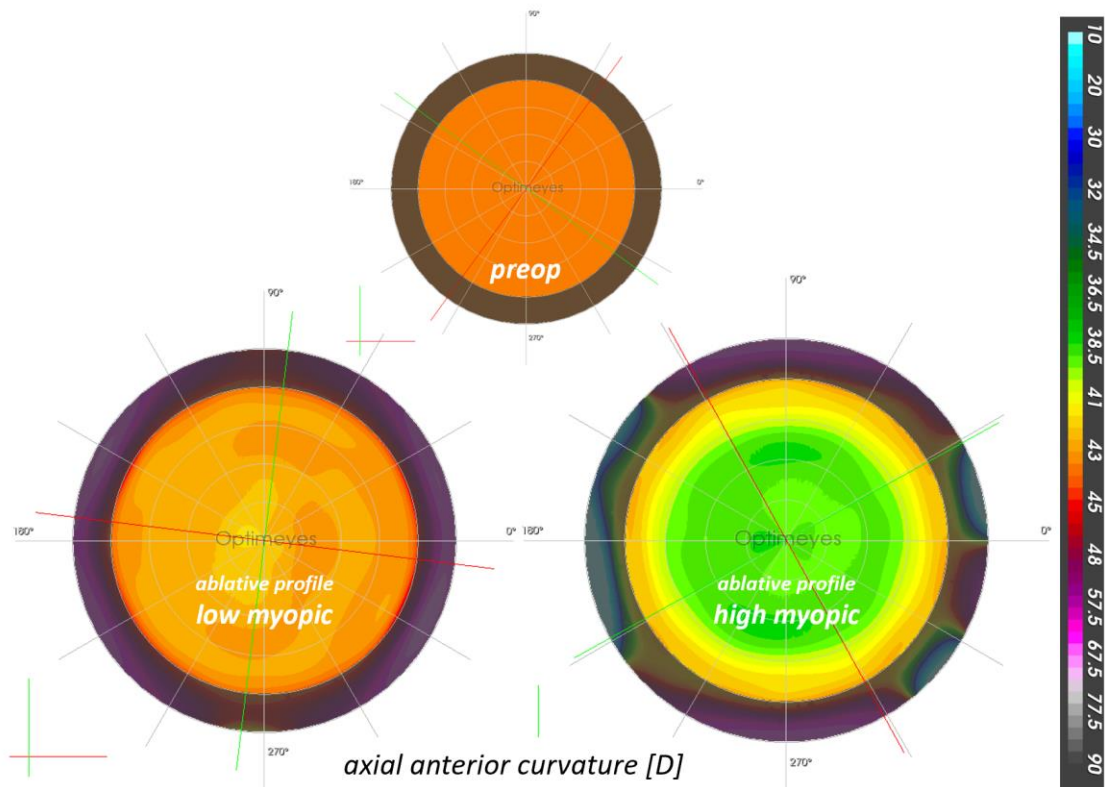


Figure 5 From the spherical preoperative surface a clear reduction in curvature can be observed. Shown are two postoperative topographies of a low myopic profile (left) and high myopic profile (right).

Figure 6 and Figure 7 show the simulation results of the parameter analysis. Interestingly, the results showed only little dependence on biomechanical stiffness variations.

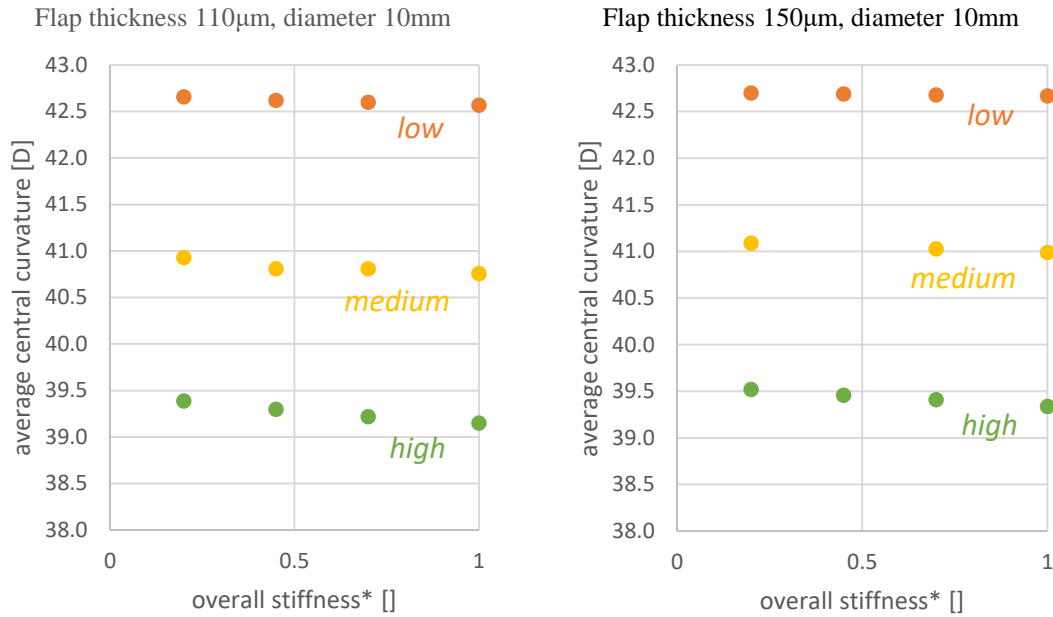


Figure 6 Simulation results show little variation with varying overall stiffness. The plot on the left side shows simulation results with a flap thickness of 110µm, and a flap diameter of 10mm. The plot on the right side shows simulation results with a flap thickness of 150µm, and a flap diameter of 10mm. All results are shown for low, medium and high myopic correction simulations.

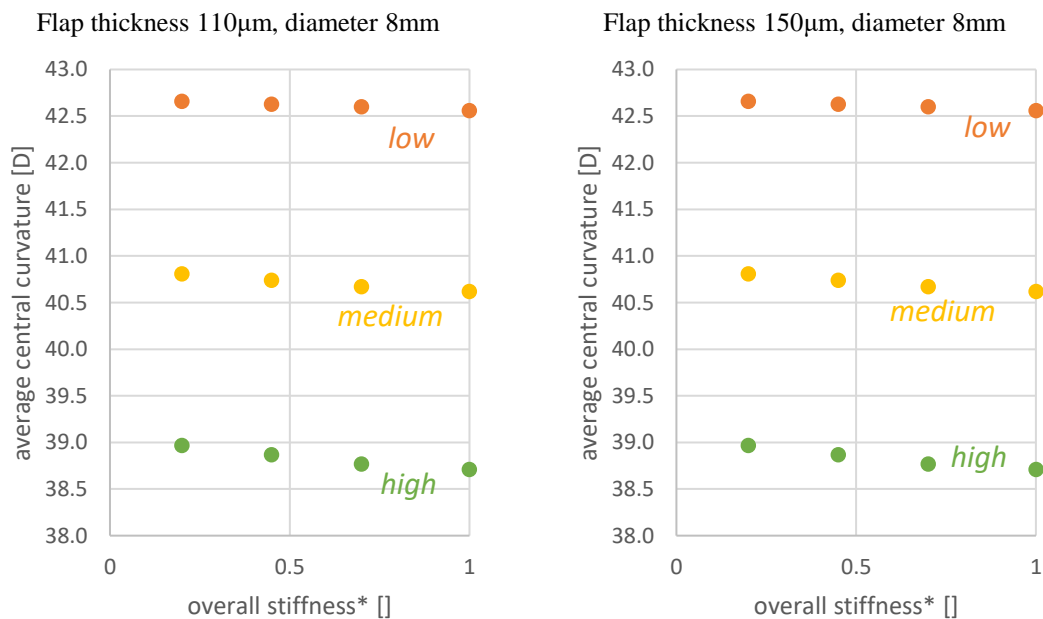


Figure 7 Simulation results show little variation with varying overall stiffness. The plot on the left side shows simulation results with a flap thickness of 110µm, and a flap diameter of 8mm. The plot on the right side shows simulation results with a flap thickness of 150µm, and a flap diameter of 8mm. All results are shown for low, medium and high myopic correction simulations.



4.2 Cataract surgery simulations

The cataract simulations were performed with the same initial model as the refractive simulations. The goal was to assess the impact of the overall corneal biomechanical stiffness changes, while also varying incision depth, incision length, and the incision position of astigmatism relaxing arcuate keratotomy incisions. Figure 8 shows example curvature maps of the corneal surface before (left), and after the simulation (right) of the arc incisions.

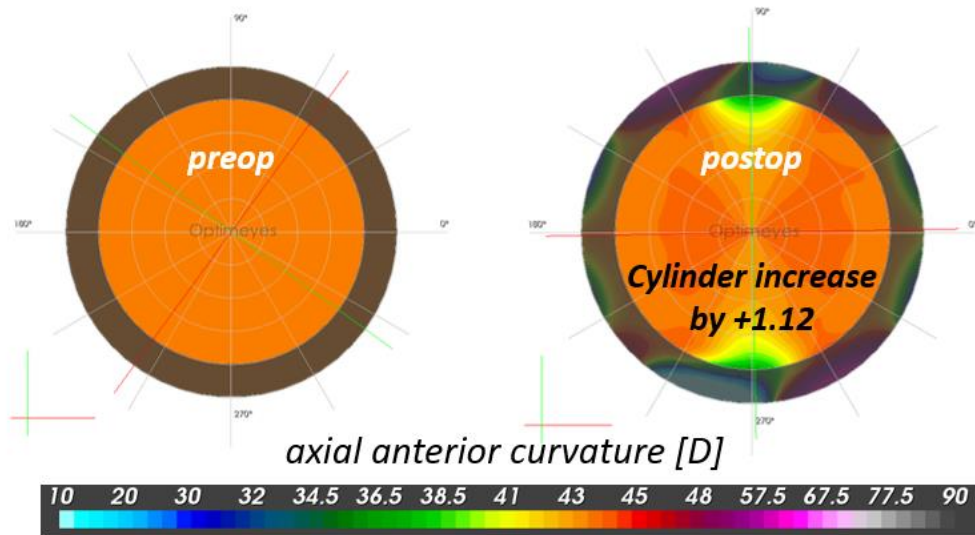
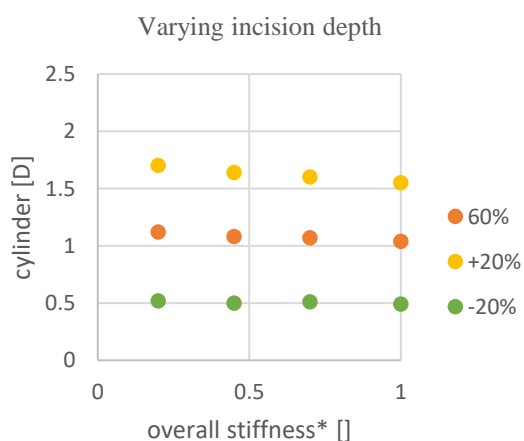


Figure 8 The spherical model before the simulation has a astigmatism cylinder value of 0.0D. After the simulation, the cylinder value is increased, because the incisosn induce astigmatism. The example case shows an induced astigmatism of 1.12D.

The results of arcuate keratotomy simulation showed very little dependence on the biomechanical stiffness of the cornea. Figure 9, Figure 10, and Figure 11 show the simulation results of varying incision depth, incision arc length, incision diameter (optical zone), and biomechanical stiffness.

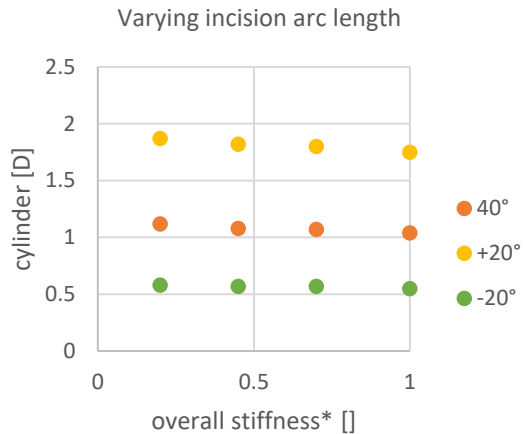


Incision parameters

Three incision depths were simulated, 40% (-20%), 60%, and 80% (+20%). The incision arc length was kept constant at 40°, and the incision diameter was kept constant at 8mm.

Figure 9 Varying incision depth from 40% to 80%, while also varying corneal biomechanical stiffness (overall stiffness). The arc length of all incisions was 40°, and the diameter (optical zone), was 8mm. The vertical axis shows the achieved chagne in astigmatism. Interestingly, the change in stiffness did not show a large effect on the simulation result.

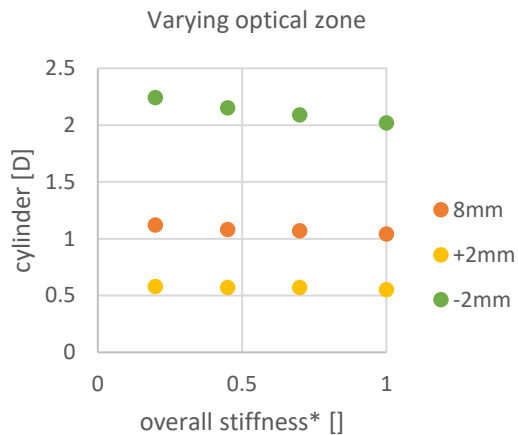




Incision parameters

Three incision arc lengths were simulated, 20° (-20°), 40°, and 60° (+20°). The incision depth was kept constant at 60%, and the incision diameter was kept constant at 8mm.

Figure 10 Varying incision arc length from 20° to 60°, while also varying corneal biomechanical stiffness (overall stiffness). The depth of all incisions was 60%, and the diameter (optical zone), was 8mm. The vertical axis shows the achieved change in astigmatism. Interestingly, the change in stiffness did not show a large effect on the simulation result.



Incision parameters

Three incision optical zones were simulated, 6mm (-2mm), 8mm, and 10mm (+2mm). The incision depth was kept constant at 60%, and the incision arc length was kept constant at 40°.

Figure 11 Varying incision optical zone from 6mm to 10mm, while also varying corneal biomechanical stiffness (overall stiffness). The depth of all incisions was 60%, and the incision arc length was 40°. The vertical axis shows the achieved change in astigmatism. Interestingly, the change in stiffness did not show a large effect on the simulation result.

4.3 ICRS Keratoconus model validation

As the purpose of using ICRSs is to flatten the corneal surface and hence reduce the corneal power, validating the FE models presented in this study could be achieved by comparing the modelled eye surface curvature with the postoperative corneal curvature. As the axial curvature assumes centres located on the corneal longitudinal axis, it always miscalculates the curvature as it moves towards the corneal periphery. It may also calculate different values at the corneal apex. Therefore, tangential curvature was selected as a validation parameter in this study. This is because of its ability to avoid the artefacts associated with the axial curvature.

Each of the 38 clinical cases' postoperative data was used to validate the relevant model by comparing the tangential curvature within the central 4 mm diameter (average pupil size (Franssen *et al.*, 2007)). The minimum error recorded was 0.01 ± 0.91 mm and the maximum was 0.72 ± 0.92 mm.

Cases Fitted with One ICRS



On one hand, when the tangential curvature averaged error (clinical R_t subtracted from model R_t) between the FE model and the clinical record was investigated against postoperative clinical parameters, this error was found to be weakly correlated with corneal horizontal radius R_h ($R=0.3$), corneal vertical radius R_v ($R=0.11$), asphericity Q ($R=0.18$), central corneal thickness (CCT) ($R=0.06$) and Sim-K ($R=0.07$).

On the other hand, when the tangential curvature averaged error between the FE model and the clinical record was examined against preoperative clinical parameters, this error was weakly correlated corneal vertical radius R_v ($R=0.04$), asphericity Q ($R=0.27$) and preoperative central corneal thickness (CCT) ($R=0.08$). Tangential curvature error was moderately correlated with the corneal horizontal radius R_h ($R=0.41$) and weakly inverse correlated with Sim-K ($R=0.08$).

Cases Fitted with Two ICRSs

When investigated against postoperative clinical parameters, the tangential curvature averaged error in the FE model was found to be strongly correlated with corneal horizontal radius R_h ($R=0.73$), moderately correlated with corneal vertical radius R_v ($R=0.65$), asphericity Q ($R=0.64$) and central corneal thickness (CCT) ($R=0.69$). Tangential curvature error was moderately inversely correlated with Sim-K only ($R=0.6$). When investigated against preoperative clinical parameters, the model was found to be strongly correlated with asphericity Q ($R=0.78$) and central corneal thickness (CCT) ($R=0.7$). Tangential curvature error was moderately correlated with corneal horizontal radius R_h ($R=0.58$), corneal vertical radius R_v ($R=0.64$) and inversely correlated with Sim-K only ($R=0.49$).

5 Conclusions

Two parametric simulation studies, one on refractive surgery and one on arcuate keratotomy, were performed. The goal was to identify the potential impact of stiffness differences in corneal tissue on surgical results. From the results obtained in these two studies, the following could be drawn:

- The use of the FE method is suitable for these tasks, but challenging. It is of great importance to achieve a high precision simulation result in order to be reliable. Most issues were observed while defining contacts between surfaces in refractive surgery simulation.
- The main finding in both parametric studies was that even though biomechanical properties were dramatically varied, the surgery simulation results were impacted only slightly.
- It will be important to compare our simulation study results with clinical data, to validate the simulation results.

The currently offered ICRS procedures have an essential limitation as the outcome of the procedure is not always clear or predicted correctly. Therefore, efforts should be made to develop a scientific method to improve the ICRS fitting practice. In the current study, an FE-based method is presented. From the result obtained in this study, the following conclusions could be drawn:

- The use of the FE method to simulate such a procedure was very challenging for many reasons. Abaqus FE software is one of the most powerful tools in the market but has



many issues in defining contact surfaces, therefore a special simulation strategy was needed, and a flexible robust MATLAB code was developed. The code changes the simulation strategy according to the Abaqus performance automatically without user intervention. This advanced approach of building a custom-built fully automated code allowed for the completion of the current study successfully.

- The key finding in terms of the simulation was the needed fixability in building FE models. This is reflected in setting the pocket opening pressure as a function of the eye IOP and adding additional stress relaxation steps automatically when needed.
- The presented FE-based method for predicting the ICRS performance of the eye was proved to be highly effective through a mathematical validation process backed by clinical investigation measurements.

6 References

- Arba Mosquera, S., Verma, S. and McAlinden, C. (2015) 'Centration axis in refractive surgery', *Eye Vis (Lond)*, 2, pp. 4.
- Bower, A. F. (2009) *Applied Mechanics of Solids*. CRC Press.
- Consejo, A., Wu, R. and Abass, A. (2020) 'Anterior Scleral Regional Variation between Asian and Caucasian Populations', *J Clin Med*, 9(11).
- Corbett, M., Maycock, N., Rosen, E. and O'Brart, D. (2019) 'Refractive Corneal Surgery': Springer International Publishing, pp. 203-234.
- Elsheikh, A., Wang, D., Brown, M., Rama, P., Campanelli, M. and Pye, D. (2007) 'Assessment of Corneal Biomechanical Properties and Their Variation with Age', *Current Eye Research*, 32(1), pp. 11-19.
- Elsheikh, A., Whitford, C., Hamarashid, R., Kassem, W., Joda, A. and Buchler, P. (2013) 'Stress free configuration of the human eye', *Med Eng Phys*, 35(2), pp. 211-6.
- Franssen, L., Tabernero, J., Coppens, J. E. and van den Berg, T. J. T. P. (2007) 'Pupil Size and Retinal Straylight in the Normal Eye', *Investigative Ophthalmology & Visual Science*, 48(5), pp. 2375-2382.
- Gross, H. (2005) 'Handbook of optical systems'. Weinheim: Wiley-VCH.
- Izquierdo, L., Mejías Smith, J. A., Lievano, J. R., Sarquis, R. and Henriquez, M. A. (2019) 'Modification of the Intrastromal Ring Position according to Postimplant Visual and Refractive Failure: Report of Two Cases', *Case Reports in Ophthalmological Medicine*, 2019, pp. 1-5.
- Kanellopoulos, A. J., Pe, L. H., Perry, H. D. and Donnenfeld, E. D. (2006) 'Modified intracorneal ring segment implantations (INTACS) for the management of moderate to advanced keratoconus. Efficacy and complications', *American Journal of Ophthalmology*, 141(3), pp. 604.
- Kolb H, F. E., Nelson R (1995) *Facts and Figures Concerning the Human Retina*. Salt Lake City (UT): University of Utah Health Sciences Center.
- Lopes, B. T., Eliasy, A., Elhalwagy, M., Vinciguerra, R., Bao, F., Vinciguerra, P., Ambrósio, R., Elsheikh, A. and Abass, A. (2021) 'Determination of Optic Axes by Corneal Topography among Italian, Brazilian, and Chinese Populations', *Photonics*, 8(2), pp. 61.
- Moore, J., Shu, X., Lopes, B. T., Wu, R. and Abass, A. (2020) 'Limbus misrepresentation in parametric eye models', *PLOS ONE*, 15(9), pp. e0236096.
- Ogden, R. W. and Hill, R. (1972) 'Large deformation isotropic elasticity - on the correlation of theory and experiment for incompressible rubberlike solids', *Proceedings*



- of the Royal Society of London. *A. Mathematical and Physical Sciences*, 326(1567), pp. 565-584.
- Sakellaris, D., Balidis, M., Gorou, O., Szentmary, N., Alexoudis, A., Grieshaber, M. C., Sagri, D., Scholl, H. and Gatzioufas, Z. (2019) 'Intracorneal Ring Segment Implantation in the Management of Keratoconus: An Evidence-Based Approach', *Ophthalmol Ther*, 8(Suppl 1), pp. 5-14.
- Smit, G. and Atchison, D. A. (1970) *The eye and visual optical instruments*. Cambridge, UK: Cambridge University Press.
- Smith, D. A. G. (2000) *Optics of the Human Eye*. Edinburgh EH13AF: Reed Educational and Professional Publishing Ltd.
- Vojnikovi, B. o. and Tamajo, E. (2013) 'Gullstrand's Optical Schematic System of the Eye Modified by Vojnikovi & Tamajo', *Coll. Antropol.*, 37 (1), pp. 41-45.
- Wang, Y. X., Xu, L., Wei, W. B. and Jonas, J. B. (2018) 'Intraocular pressure and its normal range adjusted for ocular and systemic parameters. The Beijing Eye Study 2011', *PLoS One*, 13(5), pp. e0196926.
- Whitford, C., Joda, A., Jones, S., Bao, F., Rama, P. and Elsheikh, A. (2016) 'Ex vivo testing of intact eye globes under inflation conditions to determine regional variation of mechanical stiffness', *Eye Vis (Lond)*, 3, pp. 21.
- Zhang, H., Eliasy, A., Lopes, B., Abass, A., Vinciguerra, R., Vinciguerra, P., Ambrósio, R., Jr., Roberts, C. J. and Elsheikh, A. (2021) 'Stress-Strain Index Map: A New Way to Represent Corneal Material Stiffness', *Front Bioeng Biotechnol*, 9, pp. 640434.
- Day, A., Lau, N., Stevens, J. (2016) 'Nonpenetrating femtosecond laser intrastromal astigmatic keratotomy in eyes having cataract surgery', *J Cat Refract Surg*, 42(1), pp. 102
- Pandolfi, A., Fotia, G. and Manganiello, F., (2009). 'Finite element simulations of laser refractive corneal surgery'. *Engineering with computers*, 25(1), pp.15-24.
- Petsche, S.J., Chernyak, D., Martiz, J., Levenston, M.E. and Pinsky, P.M., (2012). 'Depth-dependent transverse shear properties of the human corneal stroma'. *Investigative ophthalmology & visual science*, 53(2), pp.873-880.
- Randleman, J.B., Dawson, D.G. and Grossniklaus, H.E., (2008). 'Depth-dependent cohesive tensile strength in human donor corneas: implications for refractive surgery'. *Journal of refractive surgery*, 24(1), p.S85.
- Studer, H., Larrea, X., Riedwyl, H. and Büchler, P., (2010). 'Biomechanical model of human cornea based on stromal microstructure'. *Journal of biomechanics*, 43(5), pp.836-842.
- Søndergaard, A.P., Ivarsen, A. and Hjortdal, J., (2013). 'Corneal resistance to shear force after UVA-riboflavin cross-linking'. *Investigative ophthalmology & visual science*, 54(7), pp.5059-5069.
- Sloan, S.R., Khalifa, Y.M. and Buckley, M.R., (2014). 'The location-and depth-dependent mechanical response of the human cornea under shear loading'. *Investigative ophthalmology & visual science*, 55(12), pp.7919-7924.
- Scarcelli, G., Pineda, R. and Yun, S.H., (2012). 'Brillouin optical microscopy for corneal biomechanics'. *Investigative ophthalmology & visual science*, 53(1), pp.185-190.
- Whitford, C., Studer, H., Boote, C., Meek, K.M. and Elsheikh, A., (2015). 'Biomechanical model of the human cornea: considering shear stiffness and regional variation of collagen anisotropy and density'. *Journal of the mechanical behavior of biomedical materials*, 42, pp.76-87.



Zernike, F., (1934). 'Diffraction theory of the knife-edge test and its improved form, the phase-contrast method'. *Monthly Notices of the Royal Astronomical Society*, 94, pp.377-384.

